Journal of Alloys and Compounds 816 (2020) 152497

Contents lists available at ScienceDirect

Journal of Alloys and Compounds

journal homepage: http://www.elsevier.com/locate/jalcom

An egg holders-inspired structure design for large-volume-change anodes with long cycle life

Yunwang Zhong [a, d], Pengfei Wu [a], Shuaipeng Ge [c], Yongfeng Wu [a], Benyang Shi [a], Guangyu Shao [a], Chong Gu [a], Zhiming Su [a], Anhua Liu [a, b, d, *]

[a] College of Materials, Key Laboratory of High Performance Ceramic Fibers, Xiamen University, Xiamen, 361005, China
[b] College of Materials, Fujian Key Laboratory of Advanced Materials, Xiamen a Key Laboratory of High Performace Ceramic Fibers of Ministry of Education, College of Materials, Xiamen University, Xiamen, 361005, China
[c] Key Laboratory of Micro-nano Measurement-Manipulation and Physics, College of Physics, Beihang University, Beijing, 100191, China
[d] Shenzhen Research Institute of Xiamen University, Shenzhen, 518000, China

ARTICLE INFO

Article history:
Received 3 June 2019
Received in revised form
27 September 2019
Accepted 28 September 2019
Available online 29 September 2019

Keywords:
Egg-stacking
Secondary particles
3D carbon network
Cycling performance
Silicon anodes

ABSTRACT

Silicon has been considered as a potential alternative of anodes for advanced lithium ion battery as it possesses high capacity and abundance. However, it encounters excessive volume expansion and inferior electoral conductivity, which imposes restrictions on its further development. In order to address these two problems, yolk-shell structure is employed, in which there is a suitable void for the expansion with a shell to protect the core and promote the conductivity. Here, by the inspiration from the egg holders and inverse-opal structure, an egg-stacking-like Si/C composite (ES) anode with spherical air holes was fabricated to gather the yolk-shell particles in a 3D carbon network with abundant channels allowing electrolyte to enter the material, which can facilitate the cycling performance. The half-cell battery assembled with these anodes presents high capacity and good rate performance, with a capacity reduction of only 2–7% per current density. And the cycling performance of ES anode is also praiseworthy that it delivers a high reversible discharge capacity of 2175 mAh g^{-1} after 300 cycles at 0.5 A g^{-1}. This kind of structure design is expected to be applicative for most of large-volume-change anodes.

1. Introduction

The rapid development of high-tech industry has directly stimulated the transformation of lithium-ion batteries to the direction of high energy density, safety and efficiency, and low cost [1–3]. Among many anode materials, silicon has become the mainstream because of its ultra-high mass specific capacity and low discharge potential. However, the capacity decay and volume expansion caused by alloying reaction mechanism and the subsequent adverse consequences seriously hinder the industrialization process. For example, the volume expansion is likely to cause the pulverization and peeling of silicon particles, resulting in the electrical contact weakening and the loss of a certain amount of active material [4]. When the discharge voltage turn to about 0.7 V, the organic electrolyte can decompose and deposit on the surface of the anode material to form the solid electrolyte interface (SEI) layer. The thin SEI can promote the transmission of lithium ions, but a thick one may block the transmission of electrons and lithium ions. For silicon electrode, excessive volume expansion can cause SEI rupture and regeneration, which consumes a large number of electrolytes, hindering the occurrence of lithiation [5].

In the subsequent research, nano-silicon materials were used to solve the problem of silicon pulverization, at the same time, it can also reduce the Li^+ diffusion distance [6]. In order to solve the problem of volume expansion, it is necessary to reserve a suitable space for the silicon during the structure design process. One of the most symbolic design structures is the yolk-shell structure, in which the shell material generally choosed distinct carbon materials and some inactive materials with small volume changes, in order to ensure the stability of the SEI film outside the shell [7–9]. In addition to the diversity of material selection, the technology of void preparation has been improved [10–15].

Although silicon nanomaterials with different structures have achieved great success in improving the performance of batteries

* Corresponding author. College of Materials, Key Laboratory of High Performance Ceramic Fibers, Xiamen University, Xiamen, 361005, China.
E-mail address: ahliu@xmu.edu.cn (A. Liu).

https://doi.org/10.1016/j.jallcom.2019.152497
0925-8388/

[8], nanomaterials have larger specific surface area, which leads to more unnecessary interfacial reactions, and nanomaterials are easily agglomerated during cycling, which leads to polarization, especially at high current density, affecting rate performance and cycling life [16]. On account of the small tap density of nanomaterials, the impedance between particles is overt, resulting in poor conductivity of electrodes that is detrimentally affect the cycling life and rate performance of batteries, which in today's high current density charging and discharging requirements is extremely disadvantageous. In order to solve this problem, nano-sized silicon materials with different structures were assembled together to fabricate micron-sized secondary particles. The interfacial reaction caused by specific surface can be reduced remarkably, improving the contact between different particles, and promoting the transport of lithium ion in or into the material.

As a result, the reaction of lithium ion has high dynamic performance under high current density. Such secondary particles are rather different from micro-sized bulk silicon particles. Although the compaction density of bulk micro-particles is much larger, the transport efficiency of lithium ion in those particles is severely limited. As an advanced and productive equipment, spray drying has been used to prepare perfect secondary particles [17–19]. Acording to Guo's group, a watermelon-like silicon carbon composite negative electrode was prepared by spray drying [20]. Magnesiothermic reduction [21,22] and silicon alloys etching [23–25] are also fruitful methods to create micron-sized materials, which contain abundant voids or channels for silicon's expansion after etching. Besides the above schemes, Cui's group had prepared a self-assembly micrometer secondary particles of pomegranate-like yolk-shell nanoparticles by microemulsion method, showing excellent performance for anode electrodes [26]. Liu's team prepared graphene coated tremella-like yolk-shell micron [27], and Shuhong Yu's group reported a custard-apple-like secondary particles constituted an accumulation of yolk-shell Si/C composites [28]. This structure not only solves the problem of silicon volume expansion, but also improves the electrochemical performance of electrode materials by aggregating a large number of nanoparticles. However, the nanoparticles in the aggregated secondary particles have a larger lithium ion transport range, and each yolk-shell particle has a single point contact, which in some degree limits the lithium ion transport efficiency to the micron particles, and is not conducive to the rate performance and cycling performance [29].

Here, inspired by the structure of egg holders available in common life, a novel eggs-stacking structure for silicon/carbon composite anodes with channels for electrolyte was designed and fabricated by filtration and impregnation [30]. The preparation method of our material is borrowed from the preparation method of inverse-opal structure, which is a method to obtain regular arranged spherical air holes by removing opal template after filling with high refractive index material [31,32]. In this structure, each yolk-shell nanoparticle provides a suitable space for the volumetric expansion of silicon, and they are sequentially encapsulated by interconnected 3D carbon network frames, which effectively avoid the aggregation of silicon and improve the utilization of active sites. On the other hand, compared to the 1D and 2D morphologies, the 3D interconnected carbon network structure with spherical air holes has a large number of channels, which ensure the free penetration of electrolyte in the material, allowing every yolk-shell particle to contact with the electrolyte. At the same time, this structure can improve the efficiency of lithium ion and electron transport between particles, thereby exhibiting excellent rate performance and high current cycle performance.

2. Experimental section

2.1. Materials preparation

2.1.1. Synthesis of Si@SiO_2 particles

First, 0.3 g silicon nanoparticles were dispersed in a mixture of 70 mL deionized water, 280 mL ethanol and 5 mL ammonia (28 wt %) by sonication until a uniform mixture. Then, the mixture was stirred on a magnetic stirrer at a speed of 220 rpm at 30 °C. During the stirring process, 1 mL tetraethyl orthosilicate (TEOS) was added dropwise every 30 min for four times (total of 4 mL). After 10 h of reaction, Si@SiO_2 particles were obtained by centrifugation and alcohol washing and drying in a vacuum oven at 60 °C for 12 h.

2.1.2. Synthesis of Si@SiO_2@PDA particles

Next, 0.3 g Si@SiO_2 particles were dispersed in 300 mL (10 mM, pH = 8.5) Tris-buffer solution by sonication to form a suspension. Then 0.6 g dopamine hydrochloride was added into the suspension, and sonication was continued for 10 min, after which the mixture was stirred for 24 h at room temperature (500 rpm). Si@SiO_2@PDA particles were obtained after centrifuged, washed three times with deionized water, and dried in vacuum oven.

2.1.3. Synthesis of ES particles

The 0.3 g Si@SiO_2@PDA particles were dispersed in 30 mL deionized water to form solution A. Then the particles were transferred to a vacuum filter funnel and filtered for 3 h. At the time of 40 min before the end of the filtration, 0.03 g $NaCO_3$, 1 mL distilled water and 2.25 mL formaldehyde were put into a test tube to dissolve. 1.65 g resorcinol (RE) was added to the test tube at 20 min before the end of the filtration. After continuous ultrasound, solution B is formed, and then solution B is poured into the funnel of vacuum filtered solution A, and the filtration is continued. The total filtration time is 3 h. Then, the samples were transferred to a covered container and cured in a drying oven at 80 °C for 3 days, followed by continued curing without a cover at the same temperature for one day. The Si@SiO_2@PDA@RF composites were obtained. Finally, the silicon-carbon composites were prepared by heating up to 900 °C at 2.5 °C min^{-1} and holding for 2 h in a ceramic combustion boat inside a quartz tube filled with Ar atmosphere. The heated sample was stirred for 4 h in HCl solution (10%) and etching for half an hour in HF solution (10%) to remove SiO_2, ES was obtained. Sample SSi was processed in the same way only without the process of PDA coating.

2.2. Characterizations

The samples were characterized by X-ray diffraction (Bruker-axs XRD) to analyze the crystalline phases. The surface morphology of the samples was observed by SU-70 Thermal Field Emission Scanning Electron Microscope (SEM). Transmission Electron Microscopy (JEOL JEM-2100F) was employed to investigate the microstructure of the samples. The carbon content of the samples was measured by thermogravimetric analysis (TGA). Raman spectroscopy (Raman spectra) was used to characterize the composition of the material. The surface composition of the samples was analyzed by X-ray photoelectron spectroscopy (XPS Thermo Scientific Sigma Probe). The pore size distribution of ES was monitored by the Brunauer–Emmett–Teller (BET) method.

2.3. Electrochemical characterizations

The electrochemical performance of these samples was evaluated by using R2025 coin-type half cells with lithium foil as counter and reference electrodes. All the working electrodes were made with a uniform slurry of the active materials (70%), Super P (20%) and sodium alginate (10%) dispersed in a suitable amount of deionized water. The slurry was evenly coated on copper foil and dried in a vacuum oven at 80 °C. The mass loading of electrodes is about 0.48 mg cm^{-2}. Subsequently, the tested half cells were assembled in a glove box filled with argon. Celgard 2400 was used as the separator, with the mixture of ethylene carbonate (ED)/dimethyl carbonate (DEC)/ethylene fluorocarbonate (EFC) (volume ratio: 1:1:0.1) of 1 M $LiPF_6$ as the electrolyte. Cyclic voltammetry (CV) and electrochemical impedance spectroscopy (EIS) measurements were carried out at Autolab electrochemical workstation and the constant current charge/discharge performance was tested with Neware battery test system. To calculate the gravimetric capacity, only the quality of the silicon is taken. For CV, in order to make the selected voltage range cover the oxidation-reduction peaks of silicon and carbon, and to make the electrochemical reaction of the active material as complete as possible, we selecte the test range of 0.01−2 V [33,34] and the scanning rate is 0.5 mV S^{-1}. For EIS, a 10 mV voltage is applied in the frequency range between 100 kHz and 0.1 Hz.

3. Results and discussion

In our daily life, eggs are normally packed by egg holders, and the stacked egg holders containing channels for airiness not only can orderly fix eggs, but ensure the function of eggs' breath. Inspired by this interesting structure, we packaged the Si/C yolk-shell particles with a carbon skeleton, in which there are also numerous channels that allow electrolyte to enter the material (Fig. 1). The carbon skeleton in the structure is equivalent to the egg holders, for the yolk-shell particles can be considered as the packed eggs.

From Fig. 2a, it can be seen that all the XRD patterns of Si@SiO_2, SSi and ES present six sharp peaks at 2θ values of 28.3, 47.0, and 55.8° are corresponding to (111), (220) and (311) planes of crystalline silicon (JCPDS NO. 27−1402), respectively. Near 2θ of 24°, all of the three patterns contain a weaker and broader amorphous peak. For Si@SiO_2, this peak is due to the coating of amorphous silica on the surface of Si which was obtained by the usual sol-gel method, and the thickness of the layer could be strictly controlled by adjusting the amount of TEOS. However, both of SSi and ES were obtained after HF etching, and silicon dioxide had been completely removed. So, the amorphous peaks of SSi and ES are mainly attributed to the formation of carbon after carbonization of resorcinol-formaldehyde resin (RF) layer around the particles. According to XRD, because ES contains more amorphous carbon, the dispersive peak of ES is stronger than SSi, and the corresponding crystalline peaks of silicon are relatively weaker. It can also indirectly explain that the particles coated with PDA can fix more RF sols during the filtration process, as uncured polymer is loose with more space to absorb sols.

Fig. 1. Schematic of the materials design: yolk-shell structure, eggs-stacking structure and the digital photograph of the inspiration source.

The corresponding conclusions can also be obtained from the Raman spectra (Fig. 2b). At the Raman shift of 510 cm^{-1}, there is the standard peak of silicon, indicating that SSi and ES both contains silicon. The Raman spectra also shows that the carbon contained in the sample is amorphous carbon, because the D peak at 1352 cm^{-1} is obviously stronger than the G peak at 1596 cm^{-1}, that is, there are more defects in the carbon or irregularly arranged carbon atoms.

The silicon nanoparticles with the size distribution ranged from 40 nm to 150 nm and uniform spherical shape were purchased from Aladdin (Fig. 3a). A uniform layer of SiO_2 was coated on the surface of silicon spheres by Stöber method, and its thickness could be controlled regularly. According to a previous report [10], the void left by etching the silica layer with appropriate thickness can provide a decent space for the volume expansion of silicon. From Fig. 3b, it can be seen that the nanospheres coated with silica layer (Si@SiO_2) have a smooth surface, and still keep the previous spherical shape. Si@SiO_2 nanoparticles can be easily dispersed in deionized water, and then the dispersed solution can be vacuum filtered through a filter membrane (0.15 μm pore size) to form a uniform stacked Si@SiO_2 on the filter membrane. Since there are gaps between every two spherical particles, RF gel is gradually embedded around each Si@SiO_2 particle under the action of atmospheric pressure and capillary force. After heating treatment in an inert atmosphere, the Si@SiO_2 aggregates tightly coated with 3D carbon network can be obtained. The carbon-coated surface contains a lot of holes after etching the silica layer (Fig. 3c). Residual silicon nanoparticles can be seen in the holes, indicating that some silicon particles can be exposed on the surface of the material in the SSi prepared by this method, and then contact with the electrolyte directly during cycling, causing a large number of adverse reactions and attenuation of capacity.

In order to avoid the direct exposure of silicon to electrolyte, a layer of polydopamine (PDA) was coated on the surface of Si@SiO_2 particle before filtration, and the structure of yolk-shell particles fixed by 3D carbon network formed after pyrolysis and etching (Fig. 3e). The Si@SiO_2 particles coated with PDA exhibits a dense mass before etching and no obvious particles on the surface, indicating that more RF sols adhere to the Si@SiO_2 particles during the filtration process, resulting in higher carbon content after pyrolysis, which is also consistent with the results of XRD and Raman characterization. The etched ES particles were also characterized by SEM (Fig. 3f−h), exhibiting a lot of holes both in the cross-view and top-view images. These holes offer channels for electrolyte to enter in the material, greatly reducing the lithium ion diffusion length and increasing the efficiency of Li^+ intercalation/extraction. At the same time, due to pre-coating of PDA on Si@SiO_2 surface, silicon particles in the material exist in the form of yolk-shell structure, which avoids the direct contact between silicon and electrolyte, protecting the electrode from the loss of capacity.

The integrity of carbon coating, which plays a primary role in protecting the inner Si can be further confirmed by comparison with the results of X-ray photoelectron spectroscopy (XPS) spectrum (Fig. S1). Undressed Si nanoparticles' surface is overt from the XPS analysis, so its Si 2p signal is strongest comparing to the other two treated samples [35,36]. In addition, the prepared silicon/carbon composite secondary particle (ES) presents a weakest Si 2p signal, implying a conformal and homogeneous coating [37,38].

A transmission electron microscopy (TEM) was employed to monitor the structure of ES, guaranteeing the decent designation for the stable cycling performance. In the filtration process, RF sol

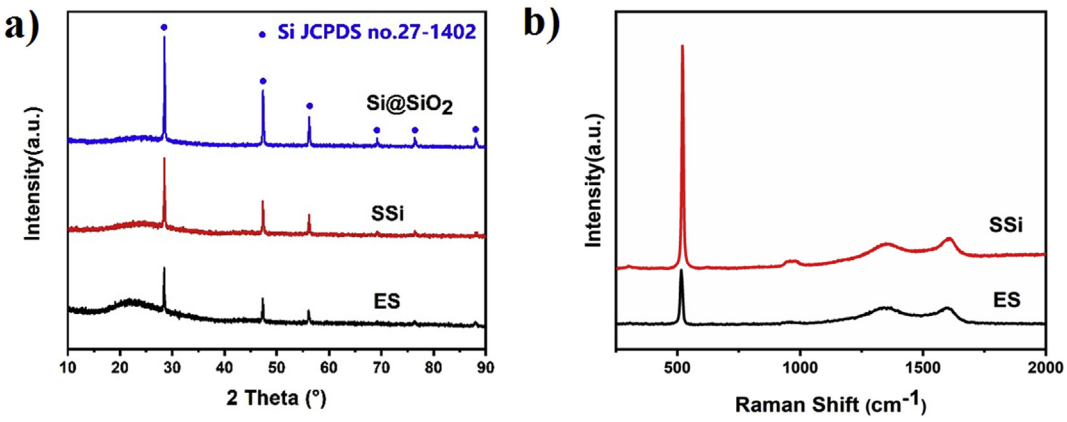

Fig. 2. a) X-ray diffraction patterns of $Si@SiO_2$, SSi and ES, and b) Raman spectra of SSi and ES.

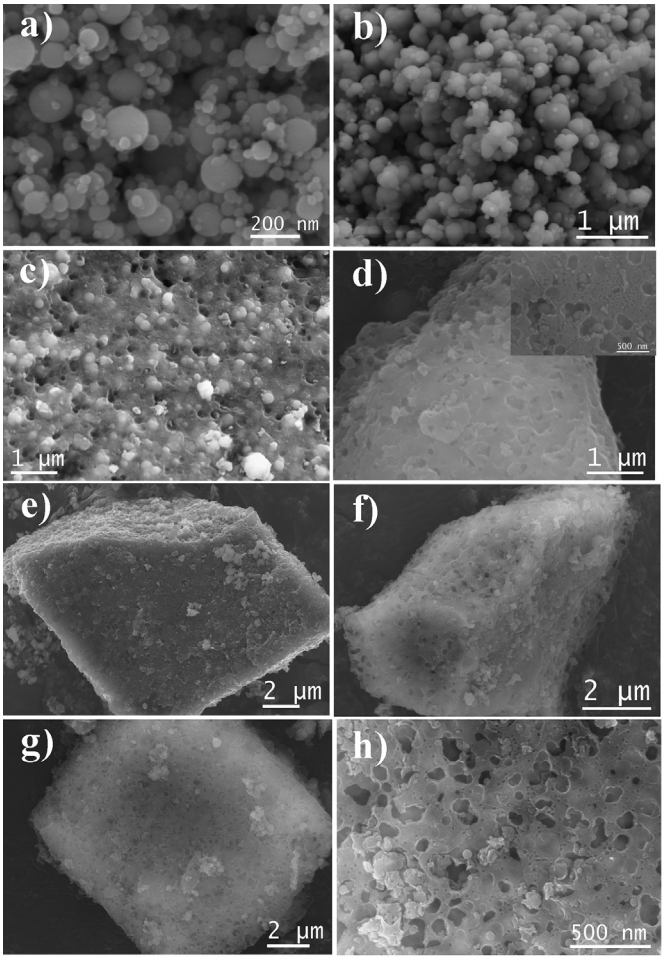

Fig. 3. a) Si, b) $Si@SiO_2$, c) SSi before etching, d) SSi (inset image is the high resolution), e) ES before etching, f) cross-view of ES, g) top-view of ES, h) high resolution of g).

can completely fill the gap between particles and fix them together to form blocky-shaped particles. These particles are about 5 μm in size, as observed by SEM. Because the silicon particles are filtered after two coatings, the silicon particles are separately dispersed in different voids, which can ensure the stability of the void to a greater extent (Fig. 4a). There are two layers of carbon outside each silicon particle, which are produced by the carbonization of PDA and RF respectively. The inner carbon layer was produced by PDA carbonization, which can be seen in TEM images to be more compact and about 15 nm (Fig. 4b). The thicker outer one was produced carbonized by RF with many pores in it that are completely different from those of SEM. The pore size in TEM is within 20 nm, while the pore size distribution shown in SEM is between 100 and 200 nm, leading to the enterance of electrolyte into the material and reduce of Li^+ diffusion length. The pore size among the outer carbon shell was further determined by BET conforming mainly about 14 nm (Fig. S2). In order to characterize the core, HRTEM was utilized to analyze its interplanar spacing, which is calculated as 0.31 nm corresponding to Si (111) (Fig. 4c).

The materials were made into electrodes and then assembled into a CR2025-type half-cell for cycling test and electrochemical characterization. Fig. 5a and Fig. S3 show the CV spectra of ES, Si and SSi at the scanning rate of 0.5 mV s^{-1} in the voltage range from 0.01 to 2.0 V, respectively. All three CVs have a reduction peak near 0.2 V, implying amorphous Li—Si alloy (a-Li_xSi) phase is formed. Correspondingly, there are two distinct oxidation peaks on the anodic curves at 0.33 V and 0.52 V, respectively, indicating that when the cells are charged to these two voltages, Li^+ are released from amorphous Li—Si alloy to form amorphous Si (a-Si) [31]. Obviously, as the silicon content decreases, the intensity of the redox peak decreases. It can be seen from the CV curves of SSi and ES that the positive electrode curve in the first cycle contain a wider peak at 0.5—0.8 V, which is due to the SEI formed by electrolyte decomposition and deposition on the surface of the material during the first discharging process. And this peak does not appear again in the subsequent two cycles, suggesting that the introduction of carbon frame makes the SEI more stable.

In order to assess the rate performance of the electrodes at different current densities (Fig. 5b and Fig. S5), every five cycles were performed at various current densities. It can be seen that, in addition to the initial 0.5 A g^{-1}, the capacity of ES slightly reduces due to activation, and it can maintain stable at the subsequent current densities. Because of the large amount of silicon exposure and electrolyte in both SSi and Si samples, the capacities of both attenuate at a gradual increase of current density. The capacity of SSi attenuates slightly slowly, probably because the carbon network structure has a certain effect on silicon nanoparticles. The discharge capacities of ES samples at different stages were investigated. It is found that there are still 953.8, 843.4, 760.9, 722.6, 669.356, 620.7, 599.1 mAh g^{-1} residual capacities after five cycles at current densities of 0.5, 1.0, 2.0, 2.0, 3.0, 5.0, 8.0, 10.0 A g^{-1}, with CE above 98%. Each change in current density only causes a 2—6% decrease in specific capacity, and when the current density restores to 0.5 A g^{-1}, the specific capacity can basically return to the original level,

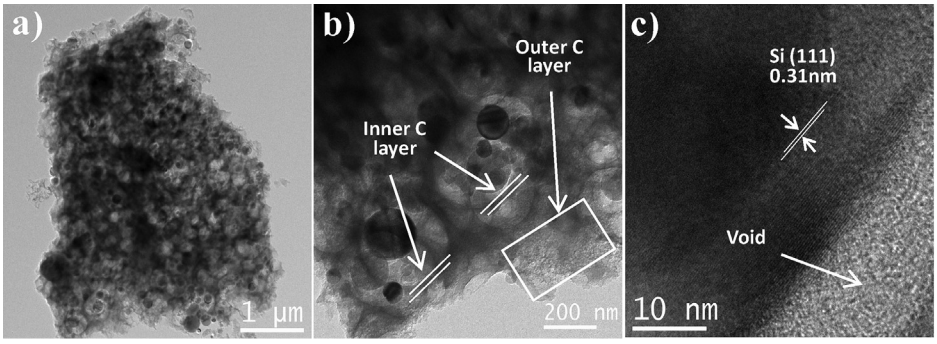

Fig. 4. a) low magnification, b) high magnification, and c) high resolution TEM images of ES.

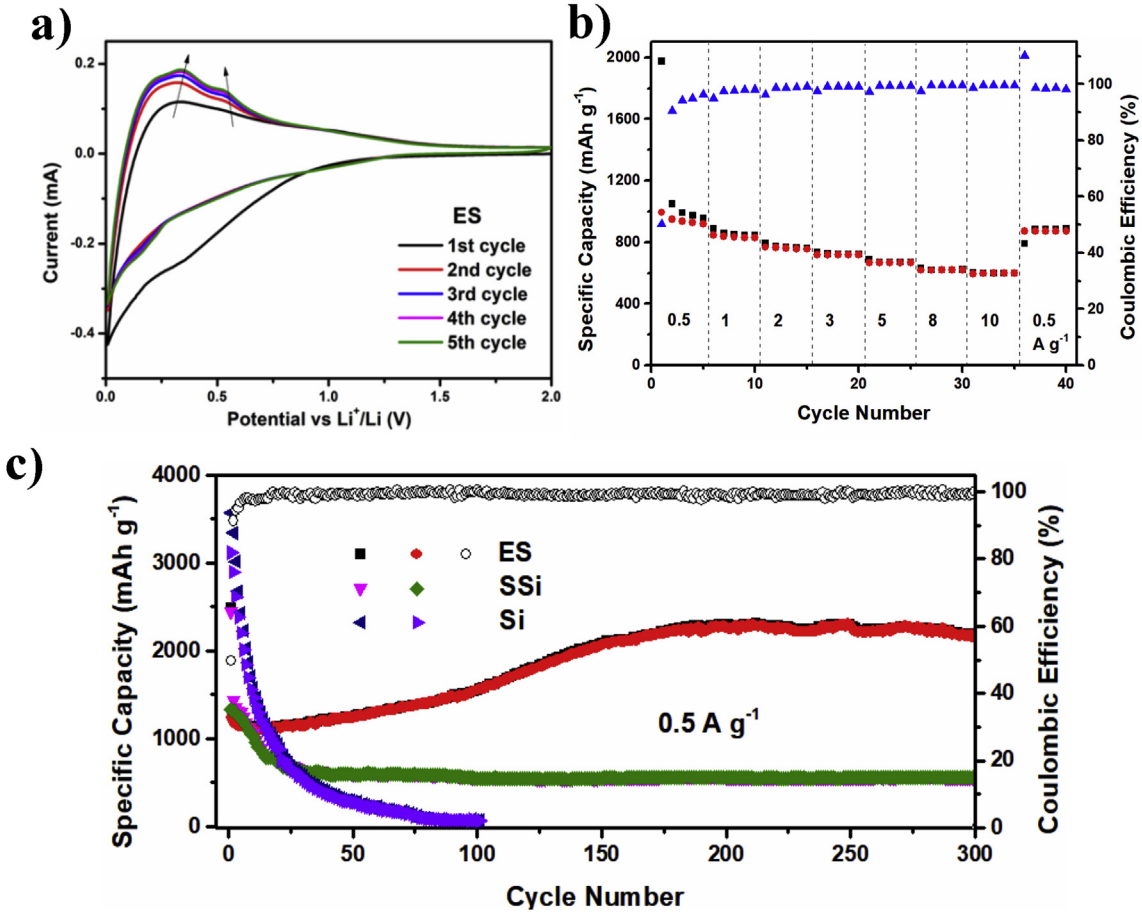

Fig. 5. Electrochemical properties of ES: a) the first five CV profiles, b) the rate performance, c) the cycling property of ES of 0.5 A g^{-1}.

indicating that ES has a very stable rate performance.

To study the direct benefit of the electrochemical performance improvement of ES, the cycling properties of Si, SSi and ES were tested between 2 and 0.01 V at a discharge/charge rate of 0.5 A g^{-1} with the initial reversible capacity around 3115, 1325, and 1237 mAh g^{-1}, respectively (Fig. 5c). For the Si and SSi, a rapid capacity decay can be seen from the very beginning of cycling, probably because of the direct exposure of active material to electrolyte. As SSi contains a 3D carbon framework to protect the silicon nanoparticles, though there are an accumulation of bare silicon surfaces, it shows a stable cycling after 30 cycles with a remanent reversible capacity of 548.5 mAh g^{-1} at the 300th cycle. In contrast, the cycling stability of ES demonstrates a substantial improvement, since it is coated with a PDA layer before filtration. It's discharge and charge capacities in the first run are around 2492.2 and 1236.8 mAh g^{-1}, meaning its Initial Coulombic Efficiency (ICE) is 49.6%. Such a high specific discharge capacity and low ICE are due to many defects in the outer carbon layer as they were obtained by grinding. These defects can capture more lithium ions in the first discharge process [39], however, some lithium ions can be permanently confined to the defects and not easily removed out, resulting in a decrease in Coulombic Efficiency [40]. It is possible to improve the ICE if the shape and size of the particles could be uniform by upgrading the preparation process and technology. There are also a decreasing to 1127.1 mAh g^{-1} within the first 21 cycles, however, the discharge capacity gradually rises to 2175 mAh g^{-1} after 300

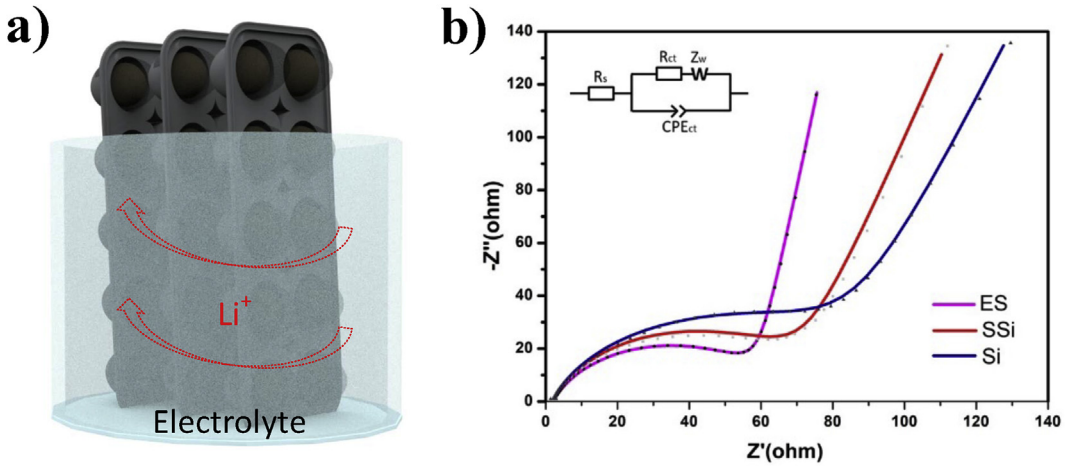

Fig. 6. a) Schematic illustrations of Li^+ transportation of ES, and b) Nyquist plots of the fresh electrodes of ES, SSi and Si.

cycles. During the first 16 cycles, the CE values are consistently below 98%, suggesting that the defects still irreversiblly capture lithium ions. So, the irreversible capacity loss of the beginning process probably because of the formation of a solid electrolyte interphase (SEI) layer and trapped Li^+ inserted into the abundant inner pores or the defects of the structure [41,42]. After 21 cycles, the capacity gradually increased, and this phenomenon was also observed in other works [43–45]. This phenomenon may be attributed to the following three points: (1) A large amount of lithium ions have been captured in the outer carbon layer in the previous few cycles. Although these lithium ions are not easy to remove out, they can improve the lithium transport capacity of the carbon layer. This results in lithium ion reaching the inner silicon core more easily in the next cycle. (2) Due to the high resistivity of Si particles, dual carbon layers and big size of sample particles, some of Si particles do not take part in the lithiation process initially, instead they become gradually activated as the electrolyte infiltrates through the carbon shells [46,47]. Different from SSi (one carbon shell) and Si (non-carbon shell), activation of the active material in ES requires a process after initial activation. The activation process leads to improved diffusion kinetics of lithium ions, and then the capacity will gradually increase. When the activation tends to be perfect, the capacity reaches a peak, then decreases slightly and tends to be stable [48,49]; (3) Lithium clusters may be formed and disappear within the structure of a 3D carbon network during the lithiation/delithiation process at lower voltages [50]. As the long cycle progresses, more defects are formed on the surface of the 3D carbon network structure, providing more active sites for Li-ion adsorption. Furthermore, It is worth noting that the Si content of ES is only 59% (Fig. S4), which suggests that the theoretical capacity of ES is only 2478 mAh g^{-1}, so that the ES anode delivers a high potential property. Table S1 offers a comparison of Si-based anodes published in this year about structure, initial specific capacities, and cycling stabilities with our study.

With the purpose of illustrating the structural advantages of egg-holders-like Si/C composite anode on electrochemical performance, the Li^+ transportation process during cycling is schematically shown in Fig. 6a. The pores emerging in 3D carbon framework throughout the whole composite particles are conducive to the free shuttle of electrolyte throughout the composites, which offers a number of accesses for the diffusion of Li^+ into the inner yolk-shell particles, narrowing the transmission distance and strengthening the specific capacity and cycling stability [51]. The inner carbon layer with plenty of about 14 nm pores is beneficial for the Li^+ transmission and protecting the inner silicon spheres. In addition, the voids provided in the yolk-shell structure are expected to accommodate a volume variation and enhance cycling stability. Consequently, the fascinating structural characteristics of the

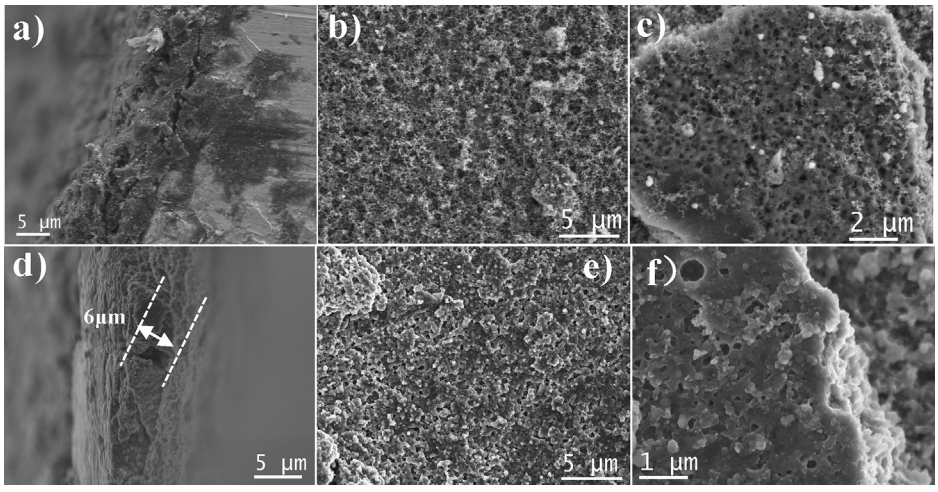

Fig. 7. SEM images of a) cross-view and b-c) top-view of ES electrodes, d) cross-view and e-f) top-view of ES electrodes after 10 cycles at a current density of 500 mA g^{-1}.

obtained multilayer porous Si/C composite films are responsible for their remarkable lithium storage properties. The advantages of this designed structure can be confirmed from the comparison of fitted EIS curves with an equivalent circuit in the inset (Fig. 6b), The Nyquist curves can be fitted by an equivalent circuit, in which the patterns consist of the semicircle in the high-middle frequency regions that is ascribed to the charge transfer resistance (R_{ct}) and the tilted line in the low frequency regions that is associated with the Warburg diffusion impedance (Z_W). In addition, the R_s stands for the bulk resistance of electrode, CPE_{ct} relates to the capacitance of interface between electrolyte and electrode, and the value of CPE is placed in Table S2. Due to the electrodes of ES, SSi and Si don't form an SEI film before the cycle, so only one semicircle was observed. The charge-transfer resistances (R_{ct}) of the Si, SSi and ES electrodes before cycling are 83, 70.18 and 56.43 Ω, respectively, suggesting that the 3D carbon network and dual carbon shells offer ES a superior conductivity [52] and enhanced charge transfer [28].

The stability of the material structure can be confirmed by comparing the morphologies of the electrodes before and after cycling. SEM images of ES electrode before and after 10 cycles at a current rate of 0.5 A g^{-1} are exhibited at Fig. 7. The change of electrode thickness can be neglected (comparing Fig. 7a and d), because the carbon structure provides a suitable volume expansion space for silicon volume expansion, so that the overall volume expansion of electrolytic materials reduces to a minimum. Comparing with top-view images (Fig. 7b and e), it can be seen that there is a dense SEI film on the surface of the electrode after cycling without appearing of cracks. Individual particles still maintain the original bulk porous morphology (Fig. 7c and f), with a reducing of the pores density and size due to the deposition of SEI, but the immersion of electrolyte into the materials is not affected.

4. Conclusion

Egg-stacking-like Si/C composite materials (ES) were fabricated by vacuum filtration to form a 3D carbon network among Si/C yolk-shell particles that we designed to gather the yolk-shell spheres plays an essential role in reducing side reaction and accelerate the transmission efficiency of Li^+ in or into the anode materials. The abundant channels in the material allow electrolyte to enter the material and further enhance the alloying/dealloying. At the same time, the unique structure of materials greatly inhibits the polarization phenomenon during cycling. These combined advantages of ES provide excellent cycling performance and rate performance, with a capacity reduction of only 2–7% per current density. The ES anode delivers a high reversible discharge capacity of 2175 mAh g^{-1} after 300 cycles at 0.5 A g^{-1}. These results confirm that the designed egg stacking-like Si/C composite materials (ES) are a promising anode material for lithium-ion batteries, while this structure design is consider as a design that most of large-volume-change anodes can draw on.

Declaration of competing interest

We declare that we do not have any commercial or associative interest that represents a conflict of interest in connection with the work submitted.

Acknowledgements

We thank the National Natural Science Foundation of China (No. 51603175), and Shenzhen Science and Technology Projects (JCYJ20180306172957494) for financial support.

Appendix A. Supplementary data

Supplementary data to this article can be found online at https://doi.org/10.1016/j.jallcom.2019.152497.

References

[1] J. Muldoon, C.B. Bucur, A.G. Oliver, T. Sugimoto, M. Matsui, H.S. Kim, G.D. Allred, J. Zajicek, Y. Kotani, Electrolyte roadblocks to a magnesium rechargeable battery, Energy Environ. Sci. 5 (2012) 5941–5950. https://doi.org/10.1039/C2EE03029B.
[2] J.P. Maranchi, A.F. Hepp, P.N. Kumta, High capacity, reversible silicon thin-film anodes for lithium-ion batteries, Electrochem. Solid State Lett. 6 (2003) A198–A201. https://doi.org/10.1149/1.1596918.
[3] I. Kovalenko, B. Zdyrko, A. Magasinski, B. Hertzberg, Z. Milicev, R. Burtovyy, I. Luzinov, G. Yushin, A major constituent of brown algae for use in high-capacity Li-ion batteries, Science 334 (2011) 75–79. https://doi.org/10.1126/science.1209150.
[4] H. Wu, G. Chan, J.W. Choi, I. Ryu, Y. Yao, M.T. Mcdowell, S.W. Lee, A. Jackson, Y. Yang, L.B. Hu, Y. Cui, Stable cycling of double-walled silicon nanotube battery anodes through solid-electrolyte interphase control, Nat. Nanotechnol. 7 (2012) 310–315. https://doi.org/10.1038/nnano.2012.35.
[5] L.F. Cui, R. Riccardo, K.C. Candace, H.L. Peng, Y. Cui, Crystalline-amorphous core-shell silicon nanowires for high capacity and high current battery electrodes, Nano Lett. 9 (2009) 491–495. https://doi.org/10.1021/nl8036323.
[6] K.X. Wang, X.H. Li, J.S. Chen, Surface and interface engineering of electrode materials for lithium-ion batteries, Adv. Mater. 27 (2015) 527–545. https://doi.org/10.1002/adma.201402962.
[7] J. Ryu, D. Hong, H.W. Lee, S. Park, Practical considerations of Si-based anodes for lithium ion battery applications, Nano Res 10 (2017) 3970–4002. https://doi.org/10.1007/s12274-017-1692-2.
[8] H. Wu, Y. Cui, Designing nanostructured Si anodes for high energy lithium ion batteries, Nano Today 7 (2012) 414–429. https://doi.org/10.1016/j.nantod.2012.08.004.
[9] Y. Jin, B. Zhu, Z.D. Lu, N. Liu, J. Zhu, Challenges and recent progress in the development of Si anodes for lithium-ion battery, Energy Mater 7 (2017), 1700715, https://doi.org/10.1002/aenm.201700715.
[10] J.P. Yang, Y.X. Wang, S.L. Chou, R.Y. Zhang, Y.F. Xu, J.W. Fan, W.X. Zhang, H.K. Liu, D.Y. Zhao, S.X. Dou, Yolk-shell silicon-mesoporous carbon anode with compact solid electrolyte interphase film for superior lithium-ion batteries, Nano Energy 18 (2015) 133–142. https://doi.org/10.1016/j.nanoen.2015.09.016.
[11] L. Pan, H.B. Wang, D.C. Gao, S.Y. Chen, L. Tan, L. Li, Facile synthesis of yolk-shell structured Si-C nanocomposites as anodes for lithium-ion batteries, Chem. Commun. 50 (2014) 5878–5880. https://doi.org/10.1039/C4CC01728E.
[12] L. Zhang, R. Rajagopalan, H.P. Guo, X.L. Hu, S.X. Dou, H.K. Liu, A green and facile way to prepare granadilla-like silicon-based anode materials for Li-ion batteries, Adv. Funct. Mater. 26 (2016) 440–446. https://doi.org/10.1002/adfm.201503777.
[13] S.Q. Chen, L.F. Shen, P.A.A. Van, J. Maier, Y. Yu, Dual-functionalized double carbon shells coated silicon nanoparticles for high performance lithium-ion batteries, Adv. Mater. 29 (2017), 1605650, https://doi.org/10.1002/adma.201605650.
[14] Q. Liu, Z. Cui, R.J. Zou, J.H. Zhang, K.B. Xu, J.Q. Hu, Surface coating constraint induced anisotropic swelling of silicon in Si–Void@SiO_x nanowire anode for lithium-ion batteries, Small 13 (2017) 1603754. https://doi.org/10.1002/smll.201603754.
[15] S.C. Guo, X. Hu, Y. Hou, Z.H. Wen, Tunable synthesis of yolk–shell porous Silicon@Carbon for optimizing Si/C-based anode of lithium-ion batteries, ACS Appl. Mater. Interfaces 9 (2017) 42084–42092. https://doi.org/10.1021/acsami.7b13035.
[16] M. Okubo, E. Hosono, J. Kim, M. Enomoto, N. Kojima, T. Kudo, H.S. Zhou, I. Honma, Nanosize effect on high-rate Li-ion intercalation in $LiCoO_2$ electrode, Chem. Soc. 129 (2007) 7444–7452. https://doi.org/10.1021/ja0681927.
[17] Y.J. Zhu, S.H. Choi, X.L. Fan, J. Shin, Z.H. Ma, M.R. Zachariah, J.W. Choi, C.S. Wang, Recent progress on spray pyrolysis for high performance electrode materials in lithium and sodium rechargeable batteries, Adv. Energy Mater. 7 (2017) 1601578. https://doi.org/10.1002/aenm.201601578.
[18] H.D. Chen, Z.L. Wang, X.H. Hou, L.J. Fu, S.F. Wang, X.Q. Hu, H.Q. Qin, Y.P. Wu, Q. Ru, X. Liu, S.J. Hu, Mass-producible method for preparation of a carbon-coated graphite@plasma nano-silicon@carbon composite with enhanced performance as lithium ion battery anode, Electrochim. Acta 249 (2017) 113–121. https://doi.org/10.1016/j.electacta.2017.07.146.
[19] Y.Y. Zhang, K. Li, P.Y. Ji, D.Q. Chen, J. Zeng, Y.Z. Sun, P. Zhang, J.B. Zhao, Silicon-multi-walled carbon nanotubes-carbon microspherical composite as high-performance anode for lithium-ion batteries, J. Mater. Sci. 52 (2017) 3630–3641. https://doi.org/10.1007/s10853-016-0503-6.
[20] Q. Xu, J.Y. Li, J.K. Sun, Y.X. Yin, L.Y. Wan, Y.G. Guo, Watermelon-inspired Si/C microspheres with hierarchical buffer structures for densely compacted lithium-ion battery anodes, Adv. Energy Mater. 7 (2017), 1601481, https://doi.org/10.1002/aenm.201601481.
[21] H. Wu, N. Du, X.X. Shi, D.R. Yang, Rational design of three-dimensional macroporous silicon as high performance Li-ion battery anodes with long cycle

life, J. Power Sources 331 (2016) 76–81. https://doi.org/10.1016/j.jpowsour.2016.09.046.
[22] H.P. Jia, J.M. Zheng, J.H. Song, L.L. Luo, R. Yi, L. Estevez, W.G. Zhao, R. Patel, X.L. Li, J.G. Zhang, A novel approach to synthesize micrometer-sized porous silicon as a high performance anode for lithium-ion batteries, Nano Energy 50 (2018) 589–597. https://doi.org/10.1016/j.nanoen.2018.05.048.
[23] X.S. Zhang, M.Y. Huang, C.F. Yang, G.L. Dai, J.J. Huang, Fabrication of porous Si/nitrogen doped carbon composite and its enhanced lithium storage capability, Mater. Chem. Phys. 201 (2017) 302–310. https://doi.org/10.1016/j.matchemphys.2017.08.026.
[24] L. Sun, F. Wang, T.T. Su, H.B. Du, Room-temperature solution synthesis of mesoporous silicon for lithium ion battery anodes, ACS Appl. Mater. Interfaces 9 (2017) 40386–40393. https://doi.org/10.1021/acsami.7b14312.
[25] H.J. Tian, X.J. Tan, F.X. Xin, C.S. Wang, W.Q. Han, Micro-sized nano-porous Si/C anodes for lithium ion batteries, Nano Energy 11 (2015) 490–499. https://doi.org/10.1016/j.nanoen.2014.11.031.
[26] N. Liu, Z.D. Lu, J. Zhao, M.T. Mcdowell, H.W. Lee, W.T. Zhao, Y. Cui, A pomegranate-inspired nanoscale design for large-volume-change lithium battery anodes, Nat. Nanotechnol. 9 (2014) 187–192. https://doi.org/10.1038/NNANO.2014.6.
[27] H.W. Mi, F. Li, S.X. Xu, Z. Li, X.Y. Chai, C.X. He, Y.L. Li, J.H. Liu, A tremella-like nanostructure of Silicon@void @graphene-Like nanosheets composite as an anode for lithium-ion batteries, Nanoscale Res. Lett. 11 (2016) 1–9. https://doi.org/10.1186/s11671-016-1414-9.
[28] R.T. Xu, G. Wang, T.F. Zhou, Q. Zhang, H.P. Cong, S. Xin, J. Rao, C.F. Zhang, Y.K. Liu, Z.P. Guo, S.H. Yu, Rational design of Si@ carbon with robust hierarchically porous custard-apple-like structure to boost lithium storage, Nano Energy 39 (2017) 253–261. https://doi.org/10.1016/j.nanoen.2017.07.007.
[29] P.F. Wu, C.Q. Guo, J.T. Han, K.R. Yu, X.C. Dong, G.H. Yue, H.J. Yue, Y. Guan, A.H. Liu, Fabrication of double core-shell Si-based anode materials with nanostructure for lithium-ion battery, RSC Adv. 8 (2018) 9094–9102. https://doi.org/10.1039/c7ra13606d.
[30] J. H Jeong, K.H. Kim, D.W. Jung, K. Kim, S.M. Lee, E.S. Oh, High-performance characteristics of silicon inverse opal synthesized by the simple magnesium reduction as anodes for lithium-ion batteries, J. Power Sources 300 (2015) 182–189. https://doi.org/10.1016/j.jpowsour.2015.09.064.
[31] A. Esmanski, G.A. Ozin, Silicon inverse-opal-based macroporous materials as negative electrodes for lithium ion batteries, Adv. Funct. Mater. 19 (2009) 1999–2010. https://doi.org/10.1002/adfm.200900306.
[32] X. Huang, J. Chen, Z.Y. Lu, H. Yu, Q.Y. Yan, H.H. Hng, Carbon inverse opal entrapped with electrode active nanoparticles as high-performance anode for lithium-ion batteries, Sci. Rep. 3 (2013) 2317. https://doi.org/10.1038/srep02317.
[33] Y.X. Wang, X.F. Wen, J. Chen, S.N. Wang, Foamed mesoporous carbon/silicon composite nanofiber anode for lithium ion batteries, J. Power Sources 281 (2015) 285–292. https://doi.org/10.1016/j.jpowsour.2015.01.184.
[34] K.X. Xiang, X.Y. Wang, M.F. Chen, Y.Q. Shen, H.B. Shu, X.K. Yang, Industrial waste silica preparation of silicon carbide composites and their applications in lithium-ion battery anode, J. Alloy. Comp. 695 (2017) 100–105. https://doi.org/10.1016/j.jallcom.2016.10.165.
[35] X.L. Li, P. Meduri, X.L. Chen, W. Qi, M.H. Engelhard, W. Xu, F. Ding, J. Xiao, W. Wang, C.M. Wang, J.G. Zhang, J. Liu, Hollow core–shell structured porous Si–C nanocomposites for Li-ion battery anodes, J. Mater. Chem. 22 (2012) 11014–11017. https://doi.org/10.1039/c2jm31286g.
[36] A. Magasinski, P. Dixon, B. Hertzberg, A. Kvit, J. Ayala, G. Yushin, High-performance lithium-ion anodes using a hierarchical bottom-up approach, Nat. Mater. 9 (2010) 353–358. https://doi.org/10.1038/NMAT2725.
[37] D.S. Jung, T.H. Hwang, S.B. Park, J.W. Choi, Spray drying method for large-scale and high-performance silicon negative electrodes in Li-ion batteries, Nano Lett. 13 (2013) 2092–2097. https://doi.org/10.1021/nl400437f.
[38] P. Nie, Z.Y. Le, G. Chen, D. Liu, X.Y. Liu, H.B. Wu, P.C. Xu, X.R. Li, F. Liu, L.M. Chang, X.G. Zhang, Y.F. Lu, Graphene caging silicon particles for high-performance lithium-ion batteries, Small 14 (2018) 1800635. https://doi.org/10.1002/smll.201800635.
[39] X.Z. Jin, H. Huang, A.M. Wu, S. Gao, M.K. Lei, J.J. Zhao, X.X. Gao, G.Z. Cao, Inverse capacity growth and pocket effect in SnS_2 semifilled carbon nanotube Anode, ACS Nano 12 (2018) 8037–8047. https://doi.org/10.1021/acsnano.8b02856.
[40] P.F. Wu, G.Y. Shao, C.Q. Guo, Y.X. Lu, X.C. Dong, Y.W. Zhong, A.H. Liu, Long cycle life, low self-discharge carbon anode for Li-ion batteries with pores and dual-doping, J. Alloy. Comp. 802 (2019) 620–627. https://doi.org/10.1016/j.jallcom.2019.06.233.
[41] R.P. Liu, C. Shen, Y. Dong, J.L. Qin, Q. Wang, J. Iocozzia, S.Q. Zhao, K.J. Yuan, C.P. Han, B.H. Li, Z.Q. Lin, Sandwich-like CNTs/Si/C nanotubes as high performance anode materials for lithium-ion batteries, J. Mater. Chem. A 6 (2018) 14797–14804. https://doi.org/10.1039/c8ta04686g.
[42] E. Yoo, J. Kim, E. Hosono, H.S. Zhou, T. Kudo, I. Honma, Large reversible Li storage of graphene nanosheet families for use in rechargeable lithium ion batteries, Nano Lett. 8 (2008) 2277–2282. https://doi.org/10.1021/nl800957b.
[43] X.H. Li, M.Q. Wu, T.T. Feng, Z.Q. Xu, J.G. Qin, C. Chen, C.Y. Tu, D.X. Wang, Graphene enhanced silicon/carbon composite as anode for high performance lithium-ion batteries, RSC Adv. 7 (2017) 48286–48293. https://doi.org/10.1039/C7RA09818A.
[44] H.J. Li, M. Lu, W.J. Han, H.B. Li, Y.C. Wu, W. Zhang, J.H. Wang, B.S. Zhang, Employing MXene as a matrix for loading amorphous Si generated upon lithiation towards enhanced lithium-ion storage, Journal of Energy Chemistry 38 (2019) 50–54. https://doi.org/10.1016/j.jechem.2018.12.020.
[45] J.L. Wu, J.H. Liu, Z. Wang, X.Z. Gong, Y. Wang, A new design for Si wears double jackets used as a high-performance lithium-ion battery anode, Chem. Eng. J. 370 (2019) 565–572. https://doi.org/10.1016/j.cej.2019.03.253.
[46] T.J. Kim, J.H. Yoon, G.R. Yi, P.J. Yoo, Si nanoparticle clusters in hollow carbon capsules (SNC@C) as lithium battery anodes: toward high initial coulombic efficiency, Nanoscale 11 (2019) 13650–13658. https://doi.org/10.1039/C9NR04074A.
[47] A.R. Park, D.Y. Son, J.S. Kim, J.Y. Lee, N.G. Park, J.H. Park, J.K. Lee, P.J. Yoo, ACS Appl. Mater. Interfaces 7 (2015) 18483–18490. https://doi.org/10.1021/acsami.5b04652.
[48] K. Mishra, J.M. Zheng, R. Patel, L. Estevez, H.P. Jia, Luo, L.L. Luo, P.Z. El-Khoury, X.L. Li, X.D. Zhou, J.G. Zhang, High performance porous Si@C anodes synthesized by low temperature aluminothermic reaction, Electrochim. Acta 269 (2018) 509–516. https://doi.org/10.1016/j.electacta.2018.02.166.
[49] Z.L. Xu, Y. Gang, M.A. Garakani, S. Abouali, J.Q. Huang, J.K. Kim, Carbon-coated mesoporous silicon microsphere anodes with greatly reduced volume expansion, J. Mater. Chem. A 4 (2016) 6098–6106. https://doi.org/10.1039/C6TA01344A.
[50] C.X. Zu, H. Li, Thermodynamic analysis on energy densities of batteries, Energy Environ. Sci. 4 (2011) 2614–2624. https://doi.org/10.1039/c0ee00777c.
[51] L. Ling, Y.T. Ma, Q.S. Xie, L.S. Wang, Q.F. Zhang, D.L. Peng, Copper-nanoparticle-induced porous Si/Cu composite films as an anode for lithium ion batteries, ACS Nano 11 (2017) 6893–6903. https://doi.org/10.1021/acsnano.7b02030.
[52] J.X. Wu, X.Y. Qin, C. Miao, Y.B. He, G.M. Liang, D. Zhou, M. Liu, C.P. Han, B.H. Li, F.Y. Kang, A honeycomb-cobweb inspired hierarchical coreeshell structure design for electrospun silicon/carbon fibers as lithium-ion battery anodes, Carbon 98 (2016) 582–591. https://doi.org/10.1016/j.carbon.2015.11.048.